3D anisotropic phase shift operators

Robert J. Ferguson and Gary F. Margrave

ABSTRACT

Phase shift operators are presented that enable plane wave propagation through media that are transversely anisotropic. These operators propagate plane waves in all three spatial dimensions for all three components, and they are developed to reside at the centre of seismic imaging and modelling by the Rayleigh-Sommerfeld approach. Numerical examples are provided for P-waves, SH-waves, and SV-waves in vertical transverse-isotropy, dipping transverse-isotropy, and horizontal isotropy (vertical fractures) are provided.

INTRODUCTION

Advances in seismic acquisition technology and high-performance computing (HPC) facilitate higher fidelity imaging and modelling, however, modelling and imaging are still either too approximate for use in complex media, (Hill, 1990, for example), or they are much too expensive to use with large data sets and / or large model spaces, (Mulder and Plessix, 2004, for example). In order to capture the highest fidelity structural and textural information from large data volumes, CREWES has begun development of a large scale seismic modelling and imaging capability that is accurate in complex media, flexible with regard to the nature of the propagating wavefield, and controllable with regard to computational cost.

Our imaging and modelling effort proceeds naturally through Rayleigh-Sommerfeld integral, (Ersoy, 2007, p. 59) formulation of wave propagation. This integral is familiar in that conventional imaging by phase shift. (Gazdag, 1978) is a special case of this more general theory, and it is unique in that wave propagation is controlled numerically by a set of phase shift operators, reflection operators, and transmission operators, (Cooper and Margrave, 2008). From a development standpoint, the Rayleigh-Sommerfeld framework offers great efficiency because seismic modelling and imaging are basically the reverse of each other and differ mainly where (and when) data are evaluated during computation.

Central to this scheme are extrapolation operators that accommodate heterogeneity and anisotropy for 3D multi component data. To achieve high accuracy and efficiency, the transform domain of temporal frequency and local slowness has a number of significant advantages. Here, *local slowness* implies localization of the global slowness transform by the process of windowing. As is well known, seismic reflectivity and anisotropy are derived from plane waves in slowness coordinates, so it is natural to remain there for analysis and numerical implementation. Further, heterogeneity, like the salt lenses of the Scotian Shelf, (Marland et al., 2006), result in caustics that are often impossible to resolve in space-time, (Hill, 1990). Where rocks are anisotropic, for example in the Canadian foothills and in the shales of the Western Canadian Sedimentary Basin (WCSB), problems with caustics can increase dramatically - especially for S waves, (Schoenberg and Helbig, 1997). Fortunately, caustics simplify in slowness coordinates, (de Hoop et al., 2000, where the slowness-frequency domain is equivalent to the $\tau \rightarrow \omega$ transform of their slowness and time domain.), and it is well known from global seismology that slowness is a powerful

analysis domain where caustics are encountered, (Shearer, 1999, pp. 42 - 44 for example).

Computationally, modelling and imaging conducted in local slowness coordinates hold the promise of high accuracy, high efficiency, plus control of the propagating mode. Seismic wavefields are extrapolated recursively through a geologic model, and reflection and transmission are modelled at each grid level in the model (forward modelling), or an imaging condition is invoked and seismic reflectivity is estimated (imaging). Unlike ray-based approaches, extrapolation ray paths are not restricted to minimum traveltimes, (Schneider, 1978) or maximum energy rays, (Nichols, 1996) for example, or any other subset of the multi-mode wavefield. This ability is similar to that of finite-difference approaches, (Bording and Lines, 1997), but computation is much more efficient, and control of the propagating mode is always retained - events can be turned on and off if desired without changing the model. Access to this domain is achieved simply through the Fast Fourier transform, (Foster and Mosher, 1992; Karl, 1989, pp. 331) so that distribution of data to the nodes of a cluster computer is "embarrassingly parallel", (Foster, 1995, Section 1.4.4 for example). That is, for a single frequency ω, the basic unit of data (a matrix) fits easily onto one computational node, and extrapolation, reflection, and transmission experiments proceed on each node independently. At the end of computation (or even during computation if desired), the monochromatic results are gathered and analyzed together.

In the following, we present a set of operators that will form the computational inner loop of seismic imaging and modelling within the Rayleigh-Sommerfeld scheme. These operators adapt automatically to dipping interfaces and tilted symmetry angles for transverse isotropy, and they do so for homogeneous 3D media. Rather than raytracing to find the required incident angles, cross products of two unit vectors are used to determine the effective incident ray parameter where one vector is parallel to the axis of TI symmetry, and the second is normal to the incident plane wave. An effective ray parameter results that is used to compute anisotropic vertical slowness. This slowness, in turn, is used to extrapolate the incident wavefield. Solutions for P-waves, SV-waves, and SH-waves are presented, and a number of 3D impulse responses for dipping, fractured media are given as a demonstration. A discussion of branch points associated with wave propagation in anisotropic media is presented, and a branch-point solution for SH-waves is provided.

THEORY

For constant frequency ω, ray parameters $\mathbf{p} = p_1\,\hat{\mathbf{i}} + p_2\,\hat{\mathbf{j}} + p_3\,\hat{\mathbf{k}}$ define a plane wave in $\mathbf{x} = x_1\,\hat{\mathbf{i}} + x_2\,\hat{\mathbf{j}} + x_3\,\hat{\mathbf{k}}$. Unit vectors $\hat{\mathbf{i}}$, $\hat{\mathbf{j}}$, and $\hat{\mathbf{k}}$ define the orthogonal coordinate system of the model space. From the scalar wave-equation, p_1, p_2 and p_3 are coupled according to

$$p_3 = \frac{1}{v}\sqrt{1 - (v\,p_1)^2 - (v\,p_2)^2}, \tag{1}$$

where v is acoustic velocity. Given vectors $\mathbf{u}$ and $\mathbf{v}$ in the plane of the plane wave, the normal $\hat{\mathbf{p}}$ to the plane wave is computed as

$$\hat{\mathbf{p}} = \frac{\mathbf{u} \times \mathbf{v}}{|\mathbf{u} \times \mathbf{v}|}, \tag{2}$$

where $\hat{\mathbf{p}}$ points in the direction of propagation of the incident plane wave. Given $\mathbf{u} = \Delta x_1\,\hat{\mathbf{i}} + 0\,\hat{\mathbf{j}} - \Delta x_3\,\hat{\mathbf{k}}$, and $\mathbf{v} = \Delta x_1\,\hat{\mathbf{i}} + \Delta x_2\,\hat{\mathbf{j}} + 0\,\hat{\mathbf{k}}$, for example, $\mathbf{u} \times \mathbf{v}$ is

$$\mathbf{u} \times \mathbf{v} = \Delta x_3\,\Delta x_2\,\hat{\mathbf{i}} + \Delta x_3\,\Delta x_1\,\hat{\mathbf{j}} + \Delta x_1\,\Delta x_2\,\hat{\mathbf{k}}. \tag{3}$$

For plane waves, write travel time in terms of p_3

$$\Delta x_j = \frac{\Delta t}{p_j} = \frac{\Delta x_3\,p_3}{p_j}, \tag{4}$$

and $\hat{\mathbf{u}} \times \hat{\mathbf{v}}$ becomes

$$\mathbf{u} \times \mathbf{v} = \Delta x_3^2\,p_3\left[\frac{1}{p_2}\,\hat{\mathbf{i}} + \frac{1}{p_1}\,\hat{\mathbf{j}} + \frac{p_3}{p_1\,p_2}\,\hat{\mathbf{k}}\right] = \frac{\Delta x_3^2\,p_3}{p_1\,p_2}\left[p_1\hat{\mathbf{i}} + p_2\hat{\mathbf{j}} + p_3\hat{\mathbf{k}}\right] \tag{5}$$

Unit normal $\hat{\mathbf{p}}$ to the incident plane wave is now computed as

$$\hat{\mathbf{p}} = \frac{\mathbf{u} \times \mathbf{v}}{|\mathbf{u} \times \mathbf{v}|} = \frac{p_1\,\hat{\mathbf{i}} + p_2\,\hat{\mathbf{j}} + p_3\,\hat{\mathbf{k}}}{\sqrt{p_1^2 + p_2^2 + p_3^2}}. \tag{6}$$

For numerical wave-propagation in the Fourier domain (k_1, k_2, ω), where k_1 and k_2 are the Fourier duals of x_1, x_2, and ω is temporal frequency, the normal $\hat{\mathbf{p}}$ to any component of the wave spectrum is available using equation 6. To see this, recall the simple relationships between slowness and wavenumber: $p_1 = \frac{k_1}{\omega}$ and $p_2 = \frac{k_2}{\omega}$ plus, equation 1 - for any plane wave $\varphi\,(k_1, k_2, \omega)$, then $\hat{\mathbf{p}}$ is defined through equation 6.

The importance of $\hat{\mathbf{p}}$ for a plane wave can be seen in its application to angle-dependent effects like anisotropy with a defined axis of symmetry. For example, for a TTI medium, dip θ and azimuth ϕ define the orientation of the azimuthal symmetry axis, and unit normal $\hat{\mathbf{a}}$ associated with the TTI symmetry plane is computed as

$$\hat{\mathbf{a}} = \sin\theta\,\cos\phi\,\hat{\mathbf{i}} + \sin\theta\,\sin\phi\,\hat{\mathbf{j}} + \cos\theta\,\hat{\mathbf{k}}, \tag{7}$$

and the effective ray parameter p_I between them is

$$p_I = \frac{\sin\theta_I}{v} = |\hat{\mathbf{p}} \times \hat{\mathbf{a}}|\,\sqrt{p_1^2 + p_2^2 + p_3^2}, \tag{8}$$

where θ_I, v and p_3 are evaluated in the incident medium. The form of the left-hand side of equation 8 is convenient for incident media that are also anisotropic. Figure 1 demonstrates the relationship between $\hat{\mathbf{p}}$ and $\hat{\mathbf{a}}$. Here, unit vector $\hat{\mathbf{a}}$ is parallel to the axis of symmetry of a TI medium, and $\hat{\mathbf{p}}$ is normal to an upwards traveling plane wave. The angle θ_I between $\hat{\mathbf{a}}$ and $\hat{\mathbf{p}}$ corresponds to the effective ray parameter p_I according to equation 8. In the notation of, (Thomsen, 1986), and following, (Kennett, 1983, pp. 236 - 237), (Udias, 1999, p. 268), P- and SV-wave in TI media are given by

$$q_\alpha = \frac{1}{2}\sqrt{\frac{2}{\beta^2} + \frac{2}{\alpha^2} - 4\,S\,p_I^2 - 4\,R}, \tag{9}$$

and

$$q_{\beta_{SV}} = \frac{1}{2}\sqrt{\frac{2}{\beta^2} + \frac{2}{\alpha^2} - 4\,S\,p_I^2 + 4\,R} \tag{10}$$

respectively, where

$$S = \left(\frac{1}{2}\,\frac{\alpha_0^2}{\beta_0^2} + \frac{1}{2}\right)\,\epsilon + 1 - \frac{\delta^*}{2}\,\left(\frac{\alpha_0}{\beta_0}\right)^2, \tag{11}$$

and

$$\begin{aligned} R \;=\; & \frac{1}{2}\Bigg[4\,p_I^4\,\left[S^2 - 2\,\epsilon - 1\right] + 4\,\left(\frac{p_I}{\beta_0}\right)^2\,\left[2\,\epsilon - S + 1\right] \\ & +4\,\left(\frac{p_I}{\alpha_0}\right)^2\,[1-S] + \beta_0^{-4} + \alpha_0^{-4} - 2\,\left(\alpha_0\,\beta_0\right)^{-2}\Bigg]^{\frac{1}{2}}. \end{aligned} \tag{12}$$

SH-wave velocity is given by

$$q_{\beta_{SH}} = \frac{1}{\beta_0^2} - p_I^2\,[2\,\gamma + 1]\,. \tag{13}$$

Equations 9, 10, and 13 give vertical slownesses for P- and S-waves respectively in coordinates defined by a vertical axis of TI symmetry. For extrapolation, however, we require q_α and q_β defined for media where the vertical axis of the numerical grid and the axis of TI symmetry are not aligned. For P-waves, and in terms of $q_{\alpha;i}$ and α_i in the incident medium and $q_{\alpha;r}$ and α_r in the refracted medium, Snell's Law may be written

$$\frac{1 - \left(\alpha_i\,q_{\alpha;i}\right)^2}{\alpha_i^2} = \frac{1 - \left(\alpha_r\,q_{\alpha;r}\right)^2}{\alpha_r^2}. \tag{14}$$

Equation 14 may then be solved for $q_{\alpha;r}$ according to

$$q_{\alpha;r}^2 = \frac{1}{\alpha_r^2} - \frac{1}{\alpha_i^2} + q_i^2. \tag{15}$$

Then, using

$$\frac{1}{\alpha_i^2} = p_1^2 + p_2^2 + q_{\alpha;i}^2, \tag{16}$$

and

$$\frac{1}{\alpha_r^2} = p_I^2 + q_\alpha^2, \tag{17}$$

where q_α is given by equation 9, the solution for $q_{\alpha;r}$ is:

$$q_{\alpha;r}^2 = q_\alpha^2 + p_I^2 - p_1^2 - p_2^2. \tag{18}$$

Similarly for the S-waves we have:

$$q_{\beta_{SV};r}^2 = q_{\beta_{SV}}^2 + p_I^2 - p_1^2 - p_2^2. \tag{19}$$

and

$$q_{\beta_{SH};r}^2 = q_{\beta_{SH}}^2 + p_I^2 - p_1^2 - p_2^2. \tag{20}$$

Note, when the axis of TI symmetry is parallel with the vertical axis of the numerical grid, $p_i^2 = p_1^2 + p_2^2$.

For an incident plane wave, equations 18, 19, and 20 determine vertical slowness for the plane wave that refracts into the lower medium, where the following Fourier integral governs extrapolation, (Gazdag, 1978)

$$\varphi_{\Delta z} = \varphi_0 \, e^{i \, \Delta z \, q \, \omega}. \tag{21}$$

Spectra $\varphi_{\Delta z}$ and φ_0 are computed according to

$$\varphi \leftrightarrow \varphi \left(k_x, k_y, \omega\right) = \frac{1}{\left(2\,\pi\right)^2} \int_{-\infty}^{\infty} P\left(x, y, t\right) \, e^{i[k_x \, x + k_y \, y - \omega \, t]} \, dx \, dy \, dt, \tag{22}$$

and subscripts 0 and Δz correspond to input and output spectra respectively. Vertical slowness q can be any of equations 18, 19, and 20. For example,

$$\varphi_{\Delta z} = \varphi_0 \, e^{i \, \Delta z \, q_{\beta_{SV};r} \, \omega} \tag{23}$$

extrapolates input wavefield φ_0 through Δz at SV-wave velocity using equation 19.

Branch points

From experience with isotropic media, it is important to track the location of branch points in anisotropic media. Branch points, basically, define the evanescent boundary where vertical slowness p_3 becomes complex. In 2D media that are isotropic, for example, the evanescent boundary occurs where $p_1 \, \alpha < 1$. With this certain knowledge, the evanescent region is defined, and steps may be taken to mitigate any numerical instability associated with this zone. In anisotropic media, the evanescent boundary is more difficult to identify - especially in dipping anisotropy. Of the three body wave-modes, the simplest to consider is SH. According to equation 13, the branch point for SH-waves is found by setting $q_{\beta_{SH}} = 0$, and then solving for $p_I = p_{bp}$ where p_{bp} is p_I at the branch point.. Then, through equation 8 and knowing $\hat{\mathbf{a}}$ in advance, the evanescent boundary for the incoming plane waves can be found.

When $q_{\beta_{SH}} = 0$, then, the solution for equation 13 gives branch point p_{bp} as

$$p_{bp}^2 = \frac{1}{\beta_0^2 \, \left[2\,\gamma + 1\right]}. \tag{24}$$

From equation 6, for a known TI orientation $\hat{\mathbf{a}}$, p_{bp} is given as

$$p_{bp}^2 = \left|\hat{\mathbf{p}} \times \hat{\mathbf{a}}\right|^2 \, \left[p_1^2 + p_2^2 + p_3^2\right], \tag{25}$$

where $\mathbf{p} = p_1\hat{\mathbf{i}} + p_2\hat{\mathbf{j}} + p_3\hat{\mathbf{k}}$ is here normal to the incident plane wave associated with branch point p_{bp}. Set equation 24 and 25 equal to each other and collect terms to get

$$1 = \beta_0^2 \, \left|\hat{\mathbf{p}} \times \hat{\mathbf{a}}\right|^2 \, \left[2\,\gamma + 1\right] \, \left[p_1^2 + p_2^2 + p_3^2\right] \tag{26}$$

The cross product in equation 27 is given explicitly as

$$\left|\hat{\mathbf{p}} \times \hat{\mathbf{a}}\right|^2 = \left| \begin{array}{ccc} p_1 & p_2 & p_3 \\ a_1 & a_2 & a_3 \end{array} \right|^2 \, \left[p_1^2 + p_2^2 + p_3^2\right]^{-1}, \tag{27}$$

and insertion into equation 26 gives a solution that is general for $\hat{\mathbf{a}}$,

$$1 = \beta_0^2 \begin{vmatrix} p_1 & p_2 & p_3 \\ a_1 & a_2 & a_3 \end{vmatrix}^2 [2\,\gamma + 1]\,. \tag{28}$$

For the specific case of $\hat{\mathbf{a}} = \hat{\mathbf{k}}$ (the TI axis is parallel to the vertical axis), the precise incident plane wave associated with p_{bp} is

$$1 = \beta_0^2 \left[p_1^2 + p_2^2\right] [2\,\gamma + 1]\,. \tag{29}$$

As numerical extrapolation proceeds for SH-waves, equation 29 determines p_2 for a given p_1.

EXAMPLE

To verify the performance of the operators described above, velocity surfaces for P-waves, SV-waves, and SH-waves in VTI, HTI, and TTI media are generated. Beginning with P-waves, Figures 2a and b show P-wave velocity as a function of inline (p_1) and cross line (p_2) ray parameters. For VTI (Figure 2a), velocity is symmetric for all azimuths with slow velocity associated with small p_1 and p_2 (small incident angles), and large velocity associated with large p_1 and p_2 (large incident angles). Figure 2b represents P-wave velocity in an HTI medium. Here, fractures are oriented along $p_1 = 0$ (90 degrees azimuth). Velocity for steep angles along the fracture direction is high. Velocity is low across fractures at large angles, and it is high for small angles. In a dipping TI medium, the P-wave velocity surface is a combination of VTI and HTI as can be seen in Figure 3a and b. In Figure 3a, the axis of TI symmetry dips at 45 degrees an points along $p_2 - 0$ (zero degrees azimuth). For steep dips in the negative direction, velocity rises steeply from the evanescent boundary to a high velocity, and then it decreases to low frequency and 45 degree dips on the positive side. It rises briefly as the angle increases beyond 45 degrees until it meets the evanescent boundary. Figures 3b demonstrate P-wave velocity for the same axis but with a 45 degree azimuth relative to $p_2 = 0$.

In Figures 4a, b, c, and d we see an example of P-wave propagation in 3D. A P-wave source is initiated, and propagation through a homogeneous VTI model is simulated (Figure 4a) where a snapshot is taken at a fixed time. The wavefield propagates farther along the in-line direction than along the vertical in this VTI medium (Figure 4a), and it is similarly fast along the cross-line direction (Figure 4b). A horizontal slice through this wavefield shows that wave propagation is symmetric about the TI axis of symmetry (Figure 4c, and the analytic wavefield (red line Figure 4d) overlies precisely the extrapolated wavefield.

Figure 5a, b, c, and d demonstrates P-wave propagation in a TTI medium. Here the axis of symmetry points along the inline direction towards 0 meters. Figure 4a shows that a slice through this wavefield along the cross-line direction is symmetric, with farthest propagation along the cross-line direction, and shorter propagation distance along depth. Figure 4b shows a slice along the in-line direction, wave propagation is asymmetric. Fourier wraparound and the branch point coincide close to in-line coordinate 1800 m and cross-line coordinate 1200 m. A horizontal slice through this wavefield is also asymmetric (Figure 4c), and the analytic curve overlies the wavefield between 1800 m and 4000 m until the branch point is encountered (Figure 4d).

In Figure 4a, b, c, and d, P-wave extrapolation in an HTI medium is explored. Fractures are vertical in this medium with fracture direction aligned with the cross-line axis. In Figure 4a, a cross section is symmetric and propagation distance is the same for all angles of incidence. Across the fracture direction (Figure 4b), propagation distance is farthest along depth and shortest along the in-line direction. A constant depth slice (Figure 4c) shows a slow direction across fractures and a fast direction along fractures, and the analytic curve (red line Figure 4d) overlies the wavefield to about 80 degrees angle of incidence. The wavefield diverges from the analytic curve, probably, because the velocity of the overburden was (effectively) higher than the slow-direction velocity of the HTI medium.

Figures 7a, b, c, and d show SV-wave velocity surfaces for VTI (Figure 7a), HTI (Figure 7b), TTI (45 degrees, Figure 7c), and TTI with a 45 degree dip and 45 degree azimuth (Figure 7d). Unlike P-wave velocity, SV-velocity for a VTI medium is low at the evanescent boundary, it increases to a maximum value at about 45 degrees, and it decreases to a low value at 0 degrees (Figure 7). For HTI, SV-velocity has nearly the reverse variation of P-wave velocity except that it begins at a low value at the evanescent boundary along the cross-line direction. When the medium is tilted, SV-wave velocity begins at the evanescent boundary at a fairly low value for steep negative dips and decreases quickly to a low value at -45 degrees (Figure 7b). From there it rises rapidly to a large value at 0 degrees, and it decreases from there rapidly to the evanescent boundary (Figure 7c). As the azimuth of the TTI axis is rotated, the velocity surface rotates accordingly (Figure 7d)a.

SV-wave fields in a VTI medium are given in Figures 9a, b, c, and d. In-line and cross-line slices demonstrate the associated fast and slow directions (Figures 9a and b), and the horizontal slice is symmetric (Figure 9c). The cross-line slice in Figure (Figure 9d) is given to show the caustics (-1000 m in-line and 1800 m cross-line, and -1000 m in-line and 3800 m cross-line) associated with propagation in TI media.

Significant SV-wave caustics are evident on Figures 10a, b, c, and d - particularly in Figure 10d. Here, the axis of TI symmetry is along the in-line direction. The wavefield is symmetric across the symmetry axis (Figure 10a), and it is strongly asymmetric across the axis direction (Figure 10b).

SV-waves in a HTI medium are demonstrated in Figures 11a, b, c, and d. Along fractures, the wavefield is symmetric and no caustics are apparent (Figure 11a). Across fractures, the higher velocity in the incident medium has cut off the wavefield at high dips (Figure 11b).

A horizontal slice through the SV-wavefield shows a pronounced fast and slow direction (along and across fractures respectively), and significant caustics are present (the crossed features pointing towards the corners of this volume (Figure 11c).

The velocity surfaces associated with SV-waves associated with VTI, HTI, and TTI media at different azimuths are similar to those of P-waves except slower (Figures 12a and b and 13), similarly the SH-wavefield performance (Figures 14 through Figures 16).

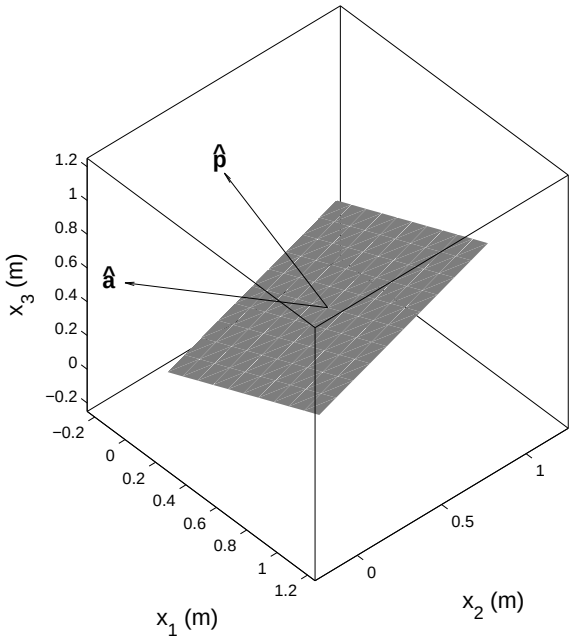

FIG. 1. For a plane wave in a TTI medium, the effective angle of incidence ϕ_I is the angle between normal $\hat{\mathbf{p}}$ to the plane wave and normal $\hat{\mathbf{a}}$ to the plane of azimuthal symmetry.

CONCLUSIONS

Designed to reside at the centre of a Rayleigh-Sommerfeld, (Ersoy, 2007, p. 59) type algorithm for seismic imaging and modelling, a number of phase shift operators for transverse isotropy are detailed and implemented. Numerical examples are presented to demonstrate wavefront extrapolation for P-waves, SV-waves, and SH-waves. Numerical artifacts are shown to be minimal for vertical transverse isotropy and horizontal transverse isotropy. In tilted transverse isotropy, numerical artifacts associated with branch points are identified. Solutions for branch points are developed for SH-waves and similar solutions are anticipated for P-waves and SV-waves. It is expected that, once an automatic process for branch point identification is determined, stabilization filter development will follow.

ACKNOWLEDGEMENTS

Thanks to the sponsors of CREWES for their support of this work.

APPENDIX A: SNAPSHOTS

In programming environments where the first value (sample) of a 1-D array corresponds to index 1, and the last sample corresponds to index N, the discrete Fourier transform is

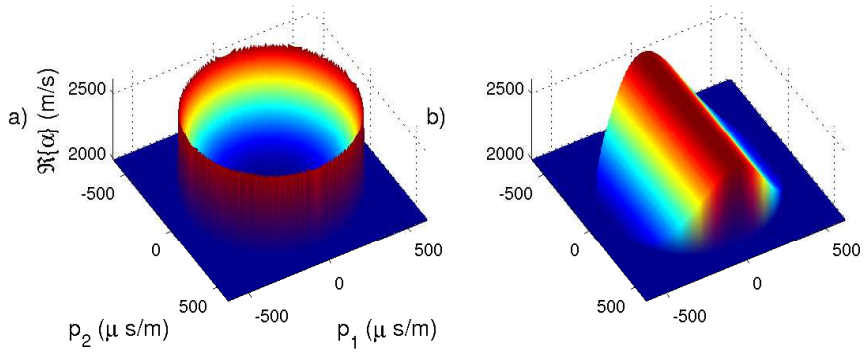

FIG. 2. P-velocity surface $(\Re\{\alpha\})$ for A VTI medium (a), and a HTI medium (b).

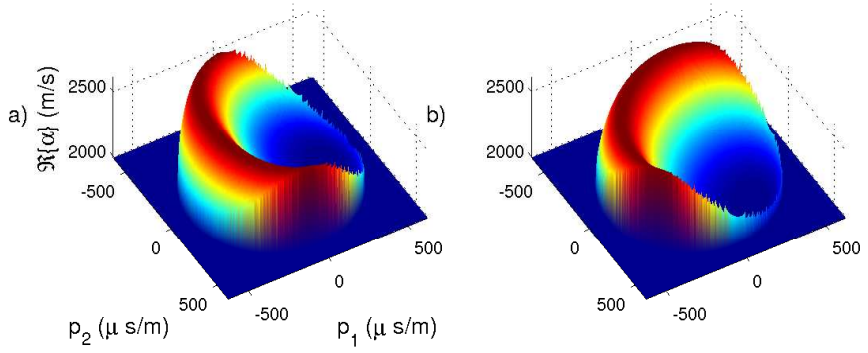

FIG. 3. P-velocity surface $(\Re\{\alpha\})$ (a) in a TTI medium ($\phi = 45$ and $\theta = 0$ degrees) and (b) for the same medium with a different azimuth ($\theta = 45$ degrees).

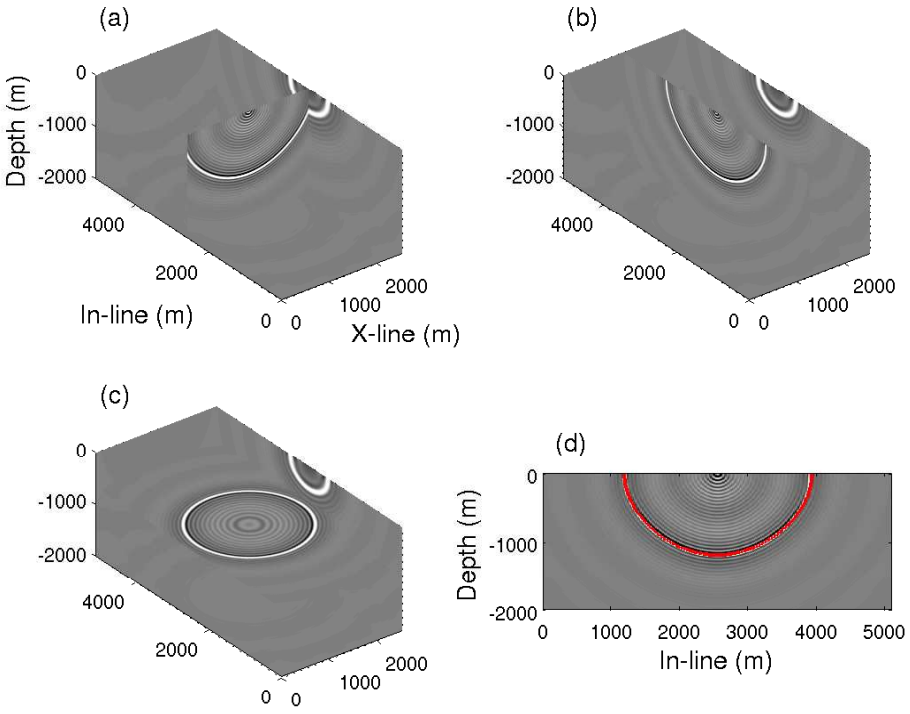

FIG. 4. 3D_z_0

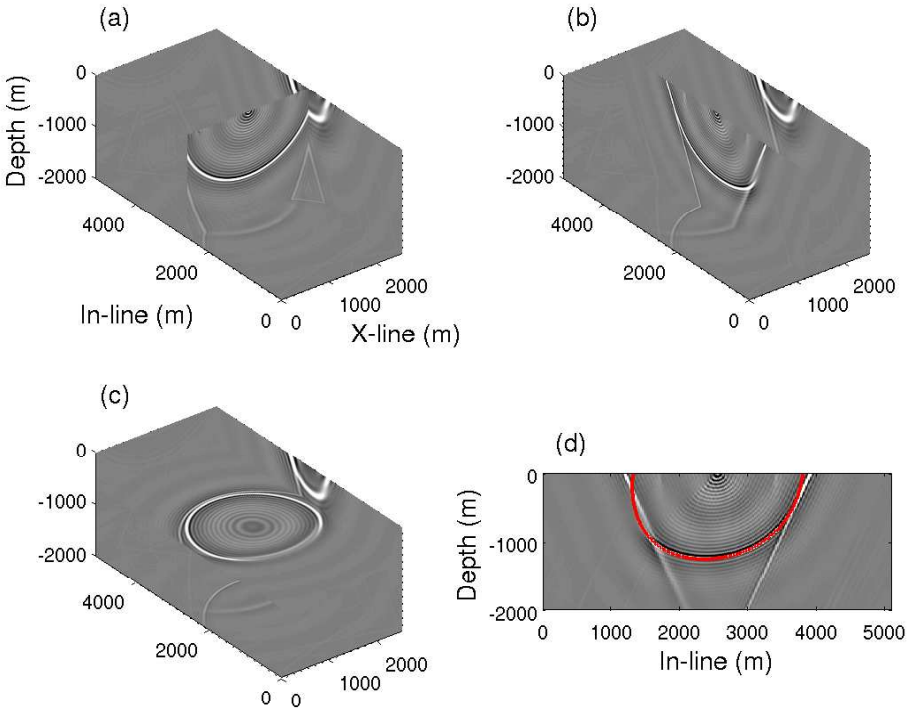

FIG. 5. 3D_z_45

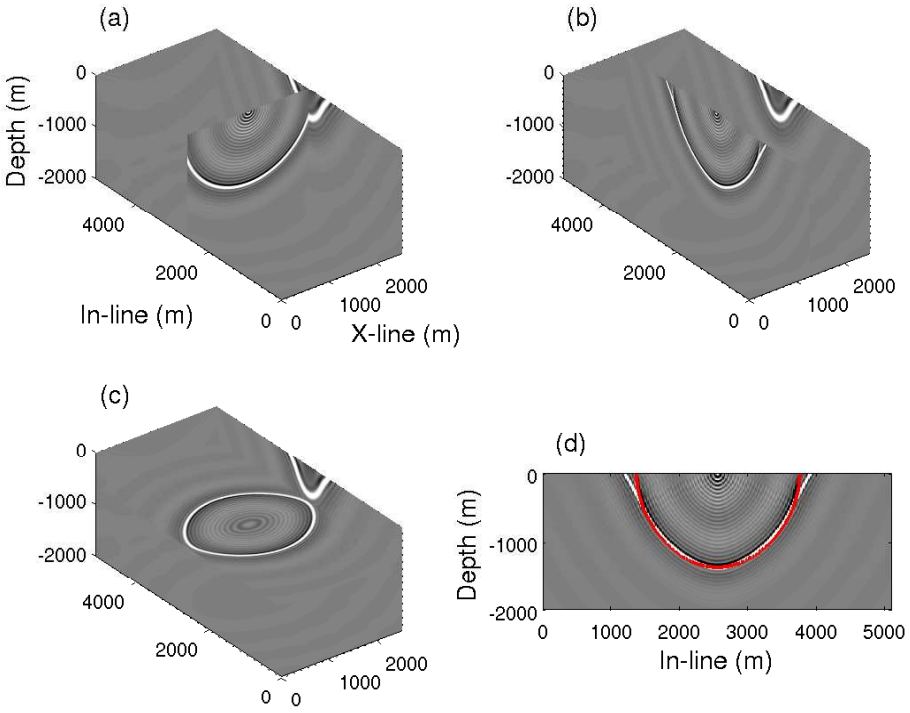

FIG. 6. 3D_z_90

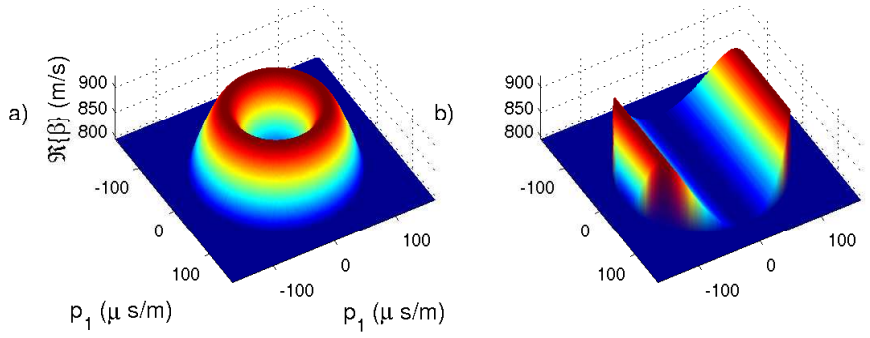

FIG. 7. SV-velocity surface $(\Re\{\beta\})$ for A VTI medium (a), and a HTI medium (b).

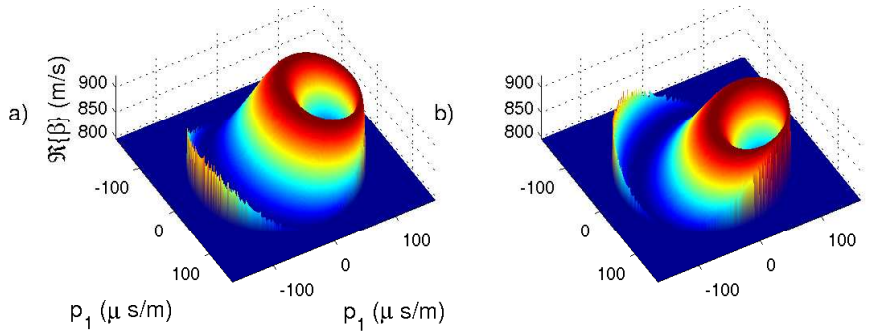

FIG. 8. SV-velocity surface $(\Re(\beta))$ in a TTI medium (a, $\phi = 45$ and $\theta = 0$ degrees) and (b) for the same medium with a different azimuth ($\theta = 45$ degrees).

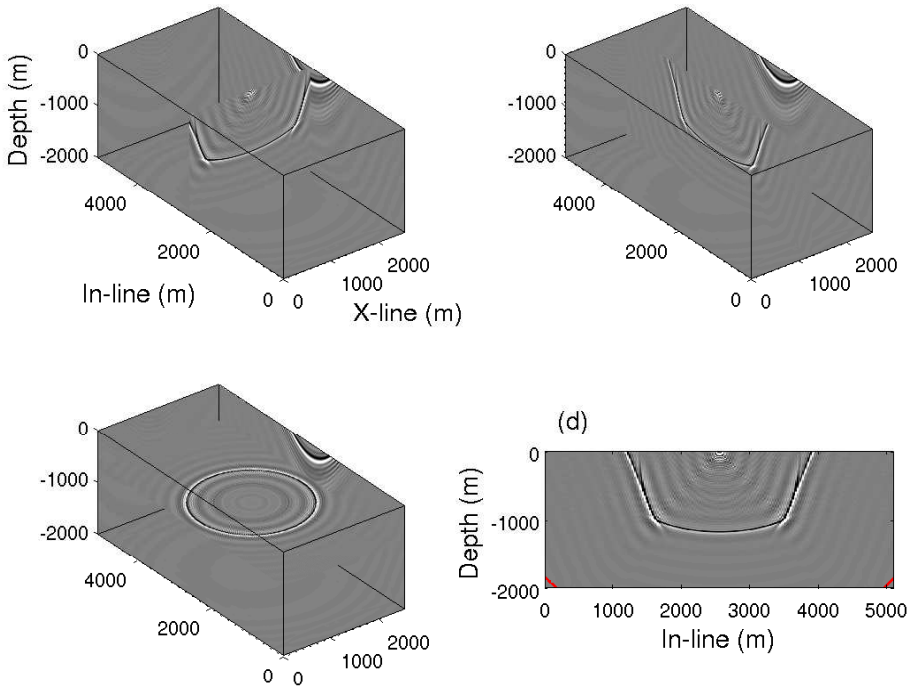

FIG. 9. 3D_z_sv_0

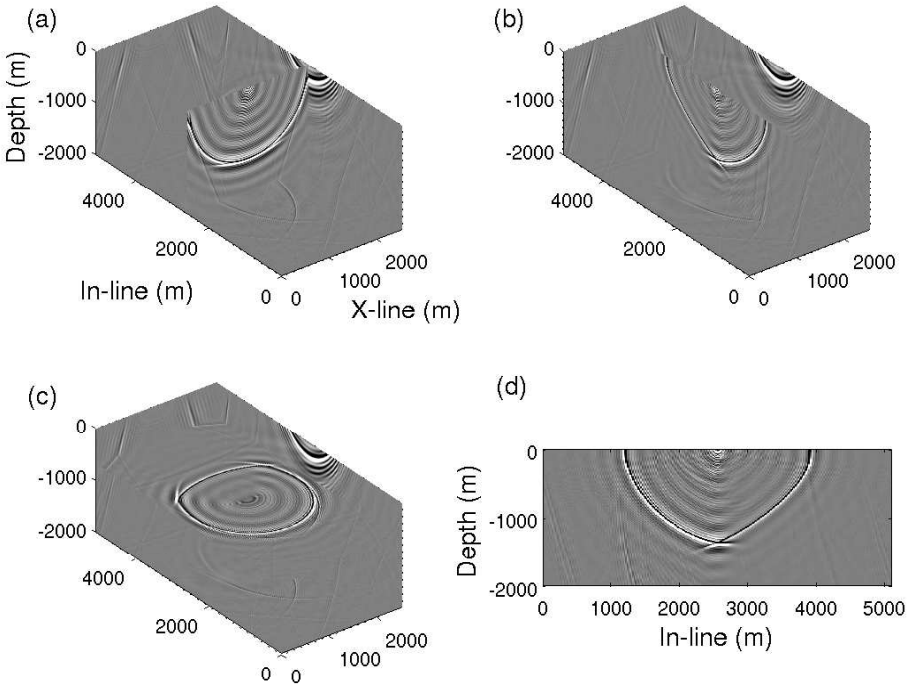

FIG. 10. 3D_z_sv_45

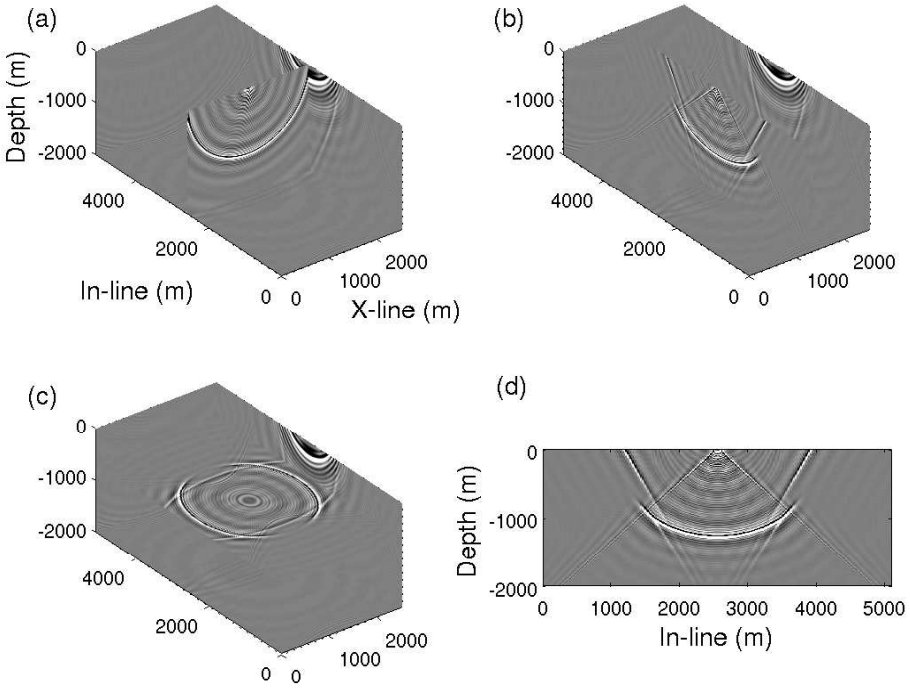

FIG. 11. 3D_z_sv_90

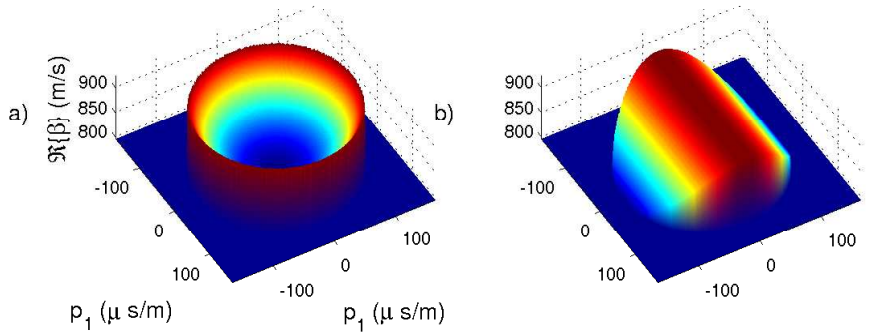

FIG. 12. SH-velocity surface $(\Re\{\beta\})$ for A VTI medium (a), and a HTI medium (b).

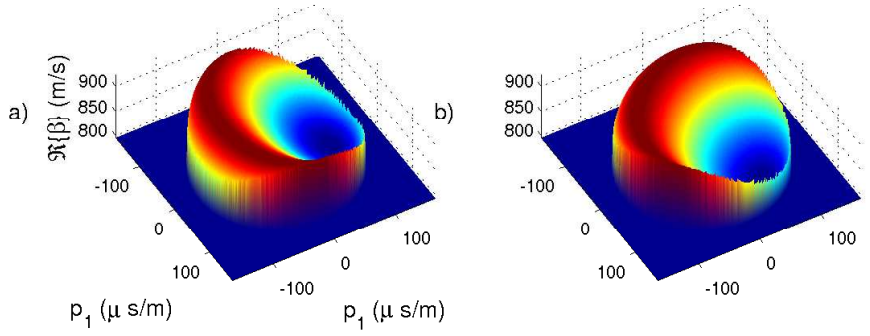

FIG. 13. SH-velocity surface $(\Re(\beta))$ in a TTI medium (a, $\phi = 45$ and $\theta = 0$ degrees) and (b) for the same medium with a different azimuth ($\theta = 45$ degrees).

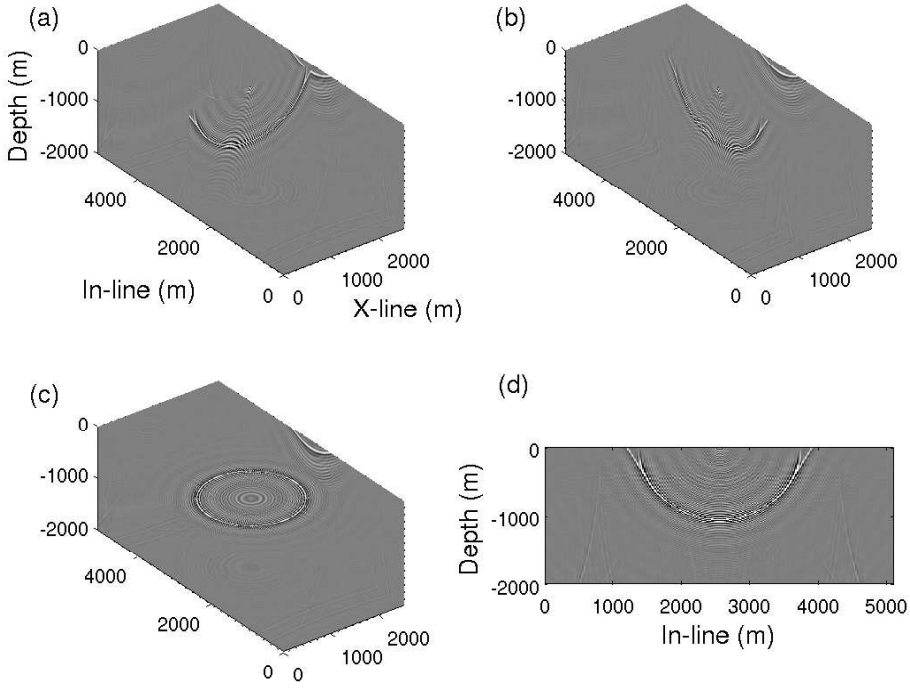

FIG. 14. 3D_z_sh_0

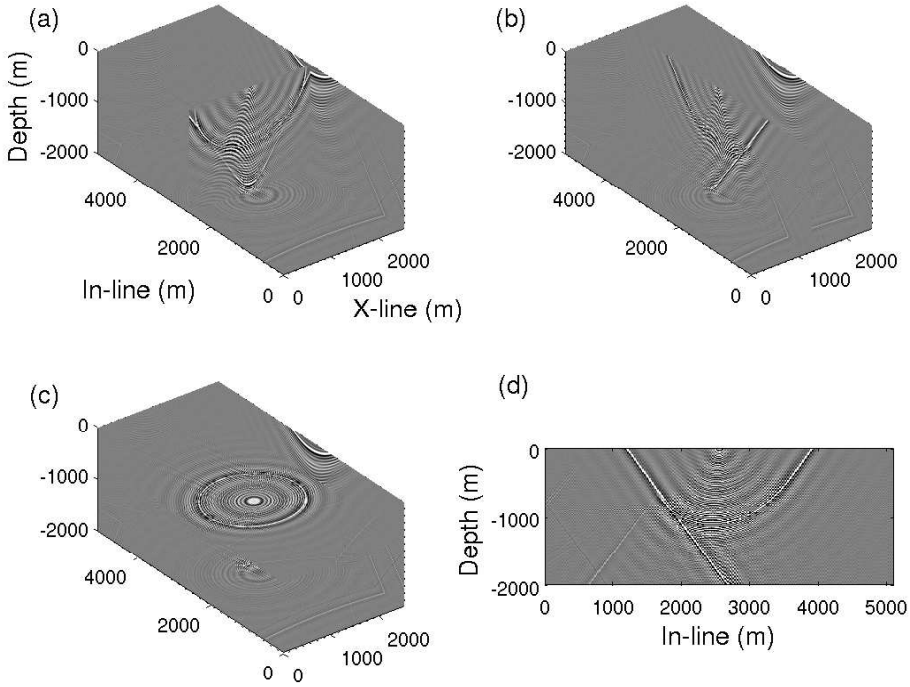

FIG. 15. 3D_z_sh_45

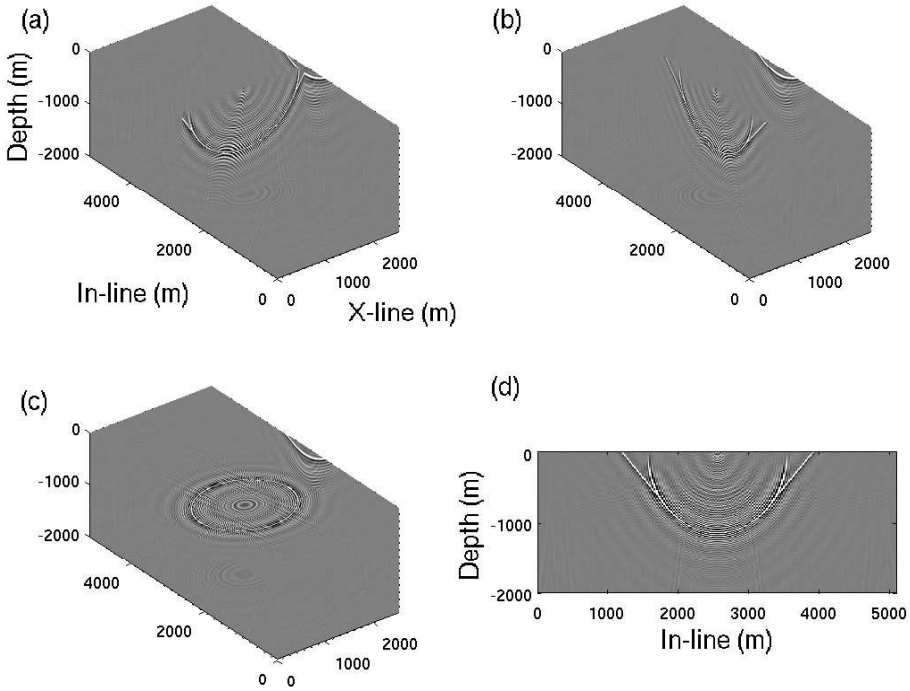

FIG. 16. 3D_z_sh_90

often given by *:

$$f_n = \frac{1}{N} \sum_{k=1}^{N} F_k \, e^{2\,\pi\,i\,\frac{[k-1]\,[n-1]}{N}}, \tag{30}$$

where f_n is the n^{th} sample of signal f, F_k is the k^{th} frequency sample of Fourier spectrum F, and N is the number of samples in f. To help us to verify the performance of the TI operator, we wish to examine a time snapshot of the propagating wavefield in $\mathbf{x}$ and x_3, and compare it to a corresponding wavefield that is computed independently. In 3D, however, equation 30 implies that we must compute a 4D dataset $(\mathbf{x}, t)$. Because we propagate wavefields in ω, we may avoid computation of an entire t axis, and compute only the 3D output $(\mathbf{x}, \tau)$, where scalar τ is time elapsed after source initiation.

So that we may take a snapshot at time τ of a propagating wave, then, we wish to modify equation 30 so that

$$n = \frac{\tau}{\Delta t} \tag{31}$$

where Δt is the time interval between samples. Further, we wish to use the symmetry properties of real, causal signals and propagate only positive frequencies to ensure computational efficiency. Equation 30, then, can be written as the sum of the inverse transform of the positive side of the spectrum and the inverse transform of the negative side according to:

$$f_n = \frac{1}{N} \sum_{k=1}^{\frac{N}{2}} F_k \, e^{2\,\pi\,i\,\frac{[k-1]\left[\frac{\tau}{\Delta t}-1\right]}{N}} + \frac{1}{N} \sum_{j=\frac{N}{2}+1}^{N} F_j \, e^{2\,\pi\,i\,\frac{[j-1]\left[\frac{\tau}{\Delta t}-1\right]}{N}}. \tag{32}$$

We note that, for equation 32 above, Fourier components F_j that correspond to negative frequencies are related to components associated with positive frequencies according to:

$$F_j = F^*_{N+2-j}, \tag{33}$$

where $\frac{N}{2} + 1 \leq j \leq N$, and where $*$ indicates complex conjugate. We then write equation 32 as

$$f_{\frac{\tau}{\Delta t}} \approx \frac{1}{N} \sum_{k=1}^{\frac{N}{2}} F_k \, e^{2\,\pi\,i\,\frac{[k-1]\left[\frac{\tau}{\Delta t}-1\right]}{N}} + \frac{1}{N} \sum_{j=\frac{N}{2}+2}^{N} F^*_{N+2-j} \, e^{2\,\pi\,i\,\frac{[j-1]\left[\frac{\tau}{\Delta t}-1\right]}{N}}, \tag{34}$$

with the $\approx$ operator to indicate that frequency component $F_{\frac{N}{2}+1}$ corresponding to negative Nyquist is never computed. Replacement of indicies simplifies equation 34 so that:

$$f_{\frac{\tau}{\Delta t}} \approx \frac{1}{N} \sum_{k=1}^{\frac{N}{2}} F_k \, e^{2\,\pi\,i\,\frac{[k-1]\left[\frac{\tau}{\Delta t}-1\right]}{N}} + \frac{1}{N} \sum_{j=2}^{\frac{N}{2}} F^*_j \, e^{2\,\pi\,i\,\frac{[N+1-j]\left[\frac{\tau}{\Delta t}-1\right]}{N}}. \tag{35}$$

*FORTRAN is an example of an environment where arrays are indexed beginning with 1. For example, the `do` loop in the following code snippet

```
do j=1,N,1
  f(j)=foo(f(j))
end do
```

begins at `j=1` and ends at `j=N`. In contrast, the same `do` loop in `C` begins with `j=0` and ends with `j=N-1`.

Then, for bandlimited data $(0 < \omega < \omega_{Nyq})$, equation 35 becomes an equality again according to:

$$f_{\frac{\tau}{\Delta t}} = \frac{1}{N} \sum_{k=a}^{b} \left[F_k \, e^{2\,\pi\,i\,\frac{[k-1]\left[\frac{\tau}{\Delta t}-1\right]}{N}} + F_k^* \, e^{2\,\pi\,i\,\frac{[N+1-k]\left[\frac{\tau}{\Delta t}-1\right]}{N}} \right]. \tag{36}$$

where $2 < a < b$ and $a < b \leq \frac{N}{2}$. Numerical implementation of equation 36 is straightforward and allows efficient computation of snapshots.

REFERENCES

Bording, R. P., and Lines, L. R., 1997, Seismic modeling and imaging with the complete wave equation: Soc. of Expl. Geophys.

Cooper, J. K., and Margrave, G. F., 2008, Seismic modelling in 3d for migration testing: Expanded Abstracts, Can. Soc. of Expl. Geophys.

de Hoop, M. V., Le Rousseau, J. H., and Wu, R. S., 2000, Generalization of the phase-screen approximation for the scattering of acoustic waves: Wave Motion, **31**, 43–70.

Ersoy, O. K., 2007, Diffraction, Fourier optics, and imaging: Wiley-Interscience.

Foster, D. J., and Mosher, C. C., 1992, Suppression of multiple reflections using the Radon transform: Geophysics, **57**, No. 03, 386–395.

Foster, I., 1995, Designing and building parallel programs: Addison-Wesley.

Gazdag, J., 1978, Wave equation migration with the phase-shift method: Geophysics, **43**, No. 07, 1342–1351.

Hill, N. R., 1990, Gaussian beam migration: Geophysics, **55**, No. 11, 1416–1428.

Karl, J. H., 1989, An introduction to digital signal processing: Academic Press.

Kennett, B. L. N., 1983, Seismic wave propagation in stratified media: Cambridge University Press.

Marland, C., Nicholas, S., Cox, W., Flannery, C., and Thistle, B., 2006, Pore pressure prediction and drilling challenges: A case study of deepwater subsalt drilling from nova scotia, canada, 21–23.

Mulder, W., and Plessix, R., 2004, A comparison between one-way and two-way wave-equation migration: Geophysics, **69**, No. 6, 1491–1504.

Nichols, D. E., 1996, Maximum energy traveltimes calculated in the seismic frequency band: Geophysics, **61**, No. 01, 253–263.

Schneider, W. A., 1978, Integral formulation for migration in two-dimensions and three-dimensions: Geophysics, **43**, No. 01, 49–76.

Schoenberg, M., and Helbig, K., 1997, Orthorhombic media: Modeling elastic wave behavior in a vertically fractured earth: Geophysics, **62**, No. 06, 1954–1974.

Shearer, P. M., 1999, Introduction to seismology: Cambridge University Press, Cambridge, Melbourne, Madrid.

Thomsen, L., 1986, Weak elastic anisotropy: Geophysics, **51**, No. 10, 1954–1966, discussion in GEO-53-04-0558-0560 with reply by author.

Udias, A., 1999, Principles of Seismology: Cambridge University Press.